AIAA JOURNAL
Vol. 47, No. 3, March 2009

Large Eddy Simulation of Plasma-Based Control Strategies for Bluff Body Flow

Donald P. Rizzetta* and Miguel R. Visbal†
U.S. Air Force Research Laboratory,
Wright–Patterson Air Force Base, Ohio 45433-7512

DOI: 10.2514/1.39168

Large eddy simulation was used to explore plasma-based control strategies for the flow past a circular cylinder in crossflow at a Reynolds number of 10,000. Solutions were obtained to the Navier–Stokes equations, using a simple phenomenological model to represent plasma-induced body forces imparted by actuators on the surrounding fluid. The numerical method used a high-fidelity time-implicit scheme, and an overset grid approach. Two fundamentally different control strategies were investigated, consisting of larger actuators that produced a wall-jet-like flow, and smaller actuators that perturbed the unstable shear layers near the separation location. The larger actuators achieved control via a "Coanda" effect, and were operated both continuously and in a pulsed manner. For pulsed cases, two different bistable states with nonzero time-mean lift were identified. All control cases resulted in at least a 50% decrease in drag, as well as elimination of oscillatory lift. Comparison is made with available experimental data for the baseline case where no control was enforced. Features of the control flowfields are described, and resultant solutions are compared with each other.

Nomenclature

A	=	plasma-force amplitude
C_d, C_l	=	cylinder drag and lift coefficients
C_p	=	pressure coefficient
D	=	cylinder diameter
D_c	=	plasma scale parameter
E	=	total specific energy
$\boldsymbol{E}$	=	nondimensional electric field vector
e_c	=	electron charge, 1.6×10^{-19} coulomb
E_{k_z}, E_ω	=	nondimensional turbulent kinetic energy wave number and frequency spectra
E_r	=	reference electric field magnitude
E_x, E_y, E_z	=	nondimensional components of the electric field vector
$\boldsymbol{F}$, $\boldsymbol{G}$, $\boldsymbol{H}$	=	inviscid vector fluxes
$\mathcal{F}$	=	nondimensional imposed actuator pulsing frequency, Df/u_∞
f	=	dimensional imposed actuator pulsing frequency, Hz
$\boldsymbol{F}_v$, $\boldsymbol{G}_v$, $\boldsymbol{H}_v$	=	viscous vector fluxes
$\mathcal{J}$	=	Jacobian of the coordinate transformation
M	=	Mach number
p	=	nondimensional static pressure
P_i	=	nondimensional actuator-integrated power-per-unit span
Pr	=	Prandtl number, 0.73 for air
$\boldsymbol{Q}$	=	vector of dependent variables
q_c	=	nondimensional charge density
$\mathcal{Q}_i$	=	components of the heat flux vector
Re	=	reference Reynolds number, $\rho_\infty u_\infty D/\mu_\infty$
$\boldsymbol{S}$	=	source vector
St	=	vortex-shedding Strouhal number
T	=	nondimensional static temperature
t	=	nondimensional time (u_∞time$/D$)
t_d	=	portion of fundamental period over which actuator is active
t_p	=	nondimensional actuator fundamental period
U, V, W	=	contravariant velocity components
u, v, w	=	nondimensional Cartesian velocity components in the x, y, z directions
u_1, u_2, u_3	=	u, v, w
x, y, z	=	nondimensional Cartesian coordinates in the streamwise, vertical, and spanwise directions
x_1, x_2, x_3	=	x, y, z
γ	=	specific heat ratio, 1.4 for air
δ_{ij}	=	Kronecker delta function
$\Delta\boldsymbol{Q}$	=	$\boldsymbol{Q}^{p+1} - \boldsymbol{Q}^p$
Δt	=	time-step size
$\Delta\theta$	=	circumferential extent of actuator
$\delta_{\xi 2}$, $\delta_{\eta 2}$, $\delta_{\zeta 2}$, $\delta_{\xi 6}$, $\delta_{\eta 6}$, $\delta_{\zeta 6}$	=	2nd-order and 6th-order finite-difference operators in ξ, η, ζ
θ	=	circumferential direction around the cylinder
μ	=	nondimensional molecular viscosity coefficient
ξ, η, ζ	=	nondimensional body-fitted computational coordinates
ξ_t, ξ_x, ξ_y, ξ_z, η_t, η_x, η_y, η_z, ζ_t, ζ_x, ζ_y, ζ_z	=	metric coefficients of the coordinate transformation
ρ	=	nondimensional fluid density
ρ_c	=	electron charge number density, $1 \times 10^{11}/\text{cm}^3$
τ_{ij}	=	components of the viscous stress tensor

Subscripts

B	=	evaluated at the cylinder base
rms	=	root-mean-square value
∞	=	dimensional reference value

Superscripts

n	=	time level
p	=	subiteration level
$\hat{}$	=	filtered value
$\bar{}$	=	time-mean quantity
$'$	=	fluctuating component

Presented as Paper 4197 at the 4th AIAA Flow Control Conference, Seattle, WA, 23–26 June 2008; received 17 June 2008; revision received 31 October 2008; accepted for publication 4 November 2008.

*Senior Research Aerospace Engineer, Computational Sciences Branch, AFRL/RBAC. Associate Fellow AIAA.

†Technical Area Leader, Computational Sciences Branch, AFRL/RBAC. Associate Fellow AIAA.

I. Introduction

SUBSONIC flows past bluff bodies, even at low Reynolds numbers, are characterized by unstable shear layers, which leave the body surface at the separation location. These shear layers then roll up into vortices that convect downstream, producing an unsteady wake. At somewhat higher Reynolds numbers, transition begins to occur in the shear layers, although the boundary layers before separation may remain laminar. This creates a more complex situation in the wake, and the appearance of fine-scale fluid structures behind the body. For sufficiently high Reynolds numbers, the boundary layers upstream of separation may already be fully turbulent.

The periodic shedding of vortices from alternate sides of a bluff body gives rise to large pressure forces exerted on the surface and correspondingly high values of drag. In addition, vortex-induced vibrations create a detrimental effect to the integrity and fatigue life of structural members found in many practical systems of engineering applications. These include air vehicle landing gear, oil drilling platforms, bridges, buildings and building towers, cables, pipelines, and heat exchange tubes, among others. The ability to control the wake behind these bodies, therefore, has a number of important implications. It can be used to reduce cycle fatigue, lower aerodynamic drag, decrease acoustic noise, and improve the flow quality for optical applications. Flow control might also be used to increase mixing and enhance combustion. Although control may be exerted by a number of both passive and active techniques, in this investigation we explore only the use of dielectric-barrier-discharge (DBD) plasma actuation.

The circular cylinder in crossflow is a canonical configuration that embodies all the common features of bluff body flows and occurs naturally in many of the aforementioned applications. Because of its geometric simplicity, cylinder flow facilitates examination of fluid phenomena and control strategies. The intricacies of cylinder flowfields have been pondered for centuries and studied extensively for over 100 years. As a representative example of bluff body flows, we consider here a cylinder in subsonic crossflow at a Reynolds number of 10,000. This flow condition displays complex shear-layer and wake dynamics but is still numerically tractable by large eddy simulation.

The technical literature is heavily populated with investigations of cylinder flows, with the majority of these being experimental. An illustrative sample of more recent works that address the shear-layer instability and transition in the near-wake region may be found in [1–7]. Among these, Williamson [5] and Ekmekci [7] provide comprehensive overviews, with the latter describing various vortex-shedding regimes and their dependence on Reynolds number. Details regarding the structure and dominant frequency of the transitional process were earlier given by Bloor [8] and Gerrard [9]. Features of the small-scale structures have been characterized by Gerrard [10], Wei and Smith [11], Filler et al. [12], Roshko [13], Chyu and Rockwell [14], Prasad and Williamson [15], and Brede [16]. These descriptions have also include effects of mechanical perturbations [12,14].

The advent of large-scale computing platforms has enabled numerical computations of transitional cylinder flows. Owing to the availability of experimental data for validation purposes, one of the most studied configurations is that for a Reynolds number of 3900. Large eddy simulations for this flow have been carried out in many investigations, some of which are documented in [17–23] A direct numerical simulation has also been performed by Ma et al. [24].

There are few cylinder calculations at Reynolds numbers higher than 3900 that do not make use of the Reynolds-averaged equations. Jordan [25] reports the large eddy simulation for a Reynolds number of 8000 and describes observed features and recorded frequencies of the transitional region. A very coarse-grid large eddy simulation at a Reynolds number of 10,000 was performed by Kalro and Tezduyar [26], where the focus was on high-performance computing. Also at this Reynolds number is the work of Dong et al. [27], which presents results of a direct numerical simulation and a comparison with the experiments of Ekmekci [7].

Although there exists a large body of experimental work regarding both active and passive control techniques for cylinder flows, many of those are beyond the scope of the present investigation and are too numerous to describe here. Some recent efforts, however, have explored the use of plasma-based devices for controlling wakes behind cylinders. The advantage of plasma-based control is that it involves no moving parts or mechanical complexity, employs no fluid supply or plumbing to deliver it, and may be activated upon demand. It has also been demonstrated that appreciable control authority may be exerted with minimal power requirements.

Asghar and Jumper [28] employed plasma actuation in order to phase synchronize vortex shedding from two cylinders placed side by side at Reynolds numbers between 8000 and 41,000. A series of experiments by McLaughlin et al. [29], Munska and McLaughlin [30], and McLaughlin et al. [31] indicated that the cylinder shedding frequency may be driven to the actuator forcing frequency by the use of plasma control. Spanwise coherence was achieved, which exhibited the lock-in behavior that had been shown with other forcing methods. Reynolds numbers up to 88,000 were considered. Plasma-based actuation has also been explored as a means for landing gear noise reduction by Thomas et al. [32,33]. Experiments performed at a Reynolds number of 33,000 showed that Karman shedding could be totally eliminated, wake turbulence levels significantly decreased, and near-field sound pressure levels substantially reduced.

The present investigation provides a companion numerical study to compliment the previously mentioned experiments in order to explore plasma-based flow-control strategies for bluff body flows. Large eddy simulation is employed to study the subsonic flow past a circular cylinder at a Reynolds number of 10,000. Two fundamentally different control approaches were considered, and both continuous and pulsed actuator operations were investigated. Grid resolution and time-step size studies were performed for the baseline case where no control was enforced, and a comparison is made with available experimental data. Features of the control flowfields are described, and resultant solutions are compared with each other and with the baseline case to indicate control effectiveness.

II. Governing Equations

The governing fluid equations are taken as the unsteady, three-dimensional, compressible, unfiltered Navier-Stokes equations. Although these computations are considered to be large eddy simulations, it will be subsequently explained why the unfiltered equations are solved. After introducing a curvilinear coordinate transformation to a body-fitted system, the equations are cast in the following nondimensional conservative form

$$\frac{\partial}{\partial t}\left(\frac{1}{\mathcal{J}}\boldsymbol{Q}\right)+\frac{\partial}{\partial \xi}\left(\boldsymbol{F}-\frac{1}{Re}\boldsymbol{F}_v\right)+\frac{\partial}{\partial \eta}\left(\boldsymbol{G}-\frac{1}{Re}\boldsymbol{G}_v\right)+\frac{\partial}{\partial \zeta}\left(\boldsymbol{H}-\frac{1}{Re}\boldsymbol{H}_v\right)=D_c q_c \boldsymbol{S} \tag{1}$$

Here t is the time, ξ, η, and ζ are the computational coordinates, $\boldsymbol{Q}$ is the vector of dependent variables, $\boldsymbol{F}$, $\boldsymbol{G}$, and $\boldsymbol{H}$ are the inviscid flux vectors, $\boldsymbol{F}_v$, $\boldsymbol{G}_v$, and $\boldsymbol{H}_v$ are the viscous flux vectors, and $\boldsymbol{S}$ is the source vector representing the effect of plasma-induced body forces. The vector of dependent variables is given as

$$\boldsymbol{Q}=[\rho \quad \rho u \quad \rho v \quad \rho w \quad \rho E]^T \tag{2}$$

the vector fluxes by

$$\boldsymbol{F} = \frac{1}{\mathcal{J}}\begin{bmatrix} \rho U \\ \rho u U + \xi_x p \\ \rho v U + \xi_y p \\ \rho w U + \xi_z p \\ \rho E U + \xi_{x_i} u_i p \end{bmatrix}, \qquad \boldsymbol{G} = \frac{1}{\mathcal{J}}\begin{bmatrix} \rho V \\ \rho u V + \eta_x p \\ \rho v V + \eta_y p \\ \rho w V + \eta_z p \\ \rho E V + \eta_{x_i} u_i p \end{bmatrix}$$

$$\boldsymbol{H} = \frac{1}{\mathcal{J}}\begin{bmatrix} \rho W \\ \rho u W + \zeta_x p \\ \rho v W + \zeta_y p \\ \rho w W + \zeta_z p \\ \rho E W + \zeta_{x_i} u_i p \end{bmatrix} \tag{3}$$

$$\boldsymbol{F}_v = \frac{1}{\mathcal{J}}\begin{bmatrix} 0 \\ \xi_{x_i}\tau_{i1} \\ \xi_{x_i}\tau_{i2} \\ \xi_{x_i}\tau_{i3} \\ \xi_{x_i}(u_j\tau_{ij} - \mathcal{Q}_i) \end{bmatrix}, \qquad \boldsymbol{G}_v = \frac{1}{\mathcal{J}}\begin{bmatrix} 0 \\ \eta_{x_i}\tau_{i1} \\ \eta_{x_i}\tau_{i2} \\ \eta_{x_i}\tau_{i3} \\ \eta_{x_i}(u_j\tau_{ij} - \mathcal{Q}_i) \end{bmatrix}$$

$$\boldsymbol{H}_v = \frac{1}{\mathcal{J}}\begin{bmatrix} 0 \\ \zeta_{x_i}\tau_{i1} \\ \zeta_{x_i}\tau_{i2} \\ \zeta_{x_i}\tau_{i3} \\ \zeta_{x_i}(u_j\tau_{ij} - \mathcal{Q}_i) \end{bmatrix} \tag{4}$$

with the source term

$$\boldsymbol{S} = \frac{1}{\mathcal{J}}\begin{bmatrix} 0 \\ E_x \\ E_y \\ E_z \\ uE_x + vE_y + wE_z \end{bmatrix} \tag{5}$$

and

$$D_c = \frac{\rho_c e_c E_r D}{\rho_\infty u_\infty^2} \tag{6}$$

where

$$U = \xi_t + \xi_{x_i} u_i, \qquad V = \eta_t + \eta_{x_i} u_i, \qquad W = \zeta_t + \zeta_{x_i} u_i \tag{7}$$

$$E = \frac{T}{\gamma(\gamma-1)M_\infty^2} + \frac{1}{2}(u^2 + v^2 + w^2) \tag{8}$$

All length scales have been nondimensionalized by the cylinder diameter D, and dependent variables have been normalized by their reference values except for p, which has been nondimensionalized by $\rho_\infty u_\infty^2$. Components of the stress tensor and heat flux vector are expressed as

$$\mathcal{Q}_i = -\left[\frac{1}{(\gamma-1)M_\infty^2}\right]\left(\frac{\mu}{Pr}\right)\frac{\partial \xi_j}{\partial x_i}\frac{\partial T}{\partial \xi_j} \tag{9}$$

$$\tau_{ij} = \mu\left(\frac{\partial \xi_k}{\partial x_j}\frac{\partial u_i}{\partial \xi_k} + \frac{\partial \xi_k}{\partial x_i}\frac{\partial u_j}{\partial \xi_k} - \frac{2}{3}\delta_{ij}\frac{\partial \xi_l}{\partial x_k}\frac{\partial u_k}{\partial \xi_l}\right) \tag{10}$$

The Sutherland law for the molecular viscosity coefficient μ and the perfect gas relationship

$$p = \frac{\rho T}{\gamma M_\infty^2} \tag{11}$$

were also employed, and Stokes' hypothesis for the bulk viscosity coefficient has been invoked.

III. Empirical Plasma Model

Many quantitative aspects of the fundamental processes governing plasma/fluid interactions remain unknown or computationally prohibitive, particularly for transitional and turbulent flows. These circumstances have given rise to the development of a wide spectrum of models with varying degrees of sophistication, which may be employed for more practical simulations. Among the simplified methods focused specifically on discharge/fluid coupling is that of Roth et al. [34,35], who associated transfer of momentum from ions to neutral particles based upon the gradient of electric pressure. A more refined approach, suitable for coupling with fluid response was an empirical model proposed by Shyy et al. [36], using separate estimates for the charge distribution and electric field. Known plasma physics parameters were linked to experimental data. This representation has been successfully employed for several previous simulations of plasma-controlled flows [37–40] and is also adopted in the present investigation.

A schematic representation of a typical single asymmetric DBD plasma actuator is depicted in Fig. 1. The actuator consists of two electrodes that are separated by a thin dielectric insulator and mounted on a body surface. An oscillating voltage, in the 10–15 kHz frequency range, is applied to the electrodes, developing an electric field about the actuator. When the imposed voltage is sufficiently high, the dielectric produces a barrier discharge, which weakly ionizes the surrounding gas. Momentum acquired by the resulting charged particles from the electric field is transferred to the primary neutral molecules by a combination of electrodynamic body forces and poorly understood complex collisional interactions. Because the bulk fluid cannot respond rapidly to the high-frequency alternating voltage, the dominant effect of actuation is to impose a time-mean electric field on the external flow. In the numerical exploration of control strategies, the entire process may be modeled as a body force vector acting on the net fluid adjacent to the actuator, which produces a flow velocity.

The model for the geometric extent of the plasma field generated by such an actuator is indicated in Fig. 2. The triangular region defined by the line segments AB, BC, and AC constitutes the plasma boundary. Outside of this region the electric field is not considered strong enough to ionize the air [36]. The electric field has its maximum value at C, and varies linearly within ABC. The peak value of the electric field is obtained from the applied voltage and the spacing between the electrodes. Along the segment AB, the electric field diminishes to its threshold value, which was taken as 30 kV/cm [36]. The electric body force is equal to $q_c\boldsymbol{E}$ and provides coupling from the plasma to the fluid, resulting in the source vector $\boldsymbol{S}$ appearing in Eq. (1). The direction of the force vector depends upon the ratio AC/BC. Within the region ABC, the charge density q_c is taken to be constant. The plasma scale parameter D_c arises from

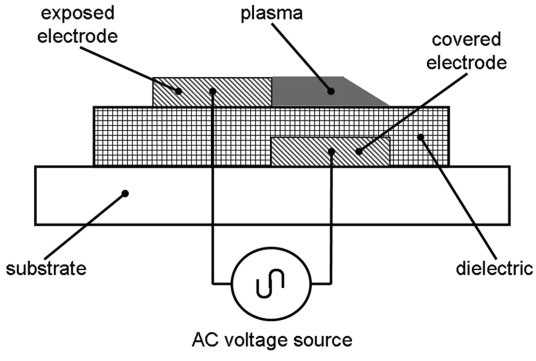

Fig. 1 Schematic representation of a plasma actuator.

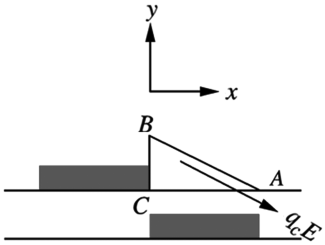

Fig. 2 Geometry for the empirical plasma-force model.

nondimensionalization of the governing equations and represents the ratio of the electrical force of the plasma to the inertial force of the fluid.

Some specific details of the plasma model incorporated in the present simulations were specified corresponding to the original experiment of Shyy et al. [36]. The ratio of the threshold electric field magnitude to its peak value was set to 0.133. Referring to Fig. 2, the distances BC and AC nondimensionalized by the cylinder diameter varied for different actuator configurations. For the purposes of the present computations, it is assumed that actuators are mounted flush with the cylinder surface and do not protrude above it. Because of empiricism of the formulation, there is some ambiguity regarding the value of the scale parameter D_c.

IV. Numerical Method

Time-accurate solutions to Eq. (1) are obtained numerically by the implicit approximately factored finite-difference algorithm of Beam and Warming [41] employing Newton-like subiterations [42], which has evolved as an efficient tool for generating solutions to a wide variety of complex fluid flow problems and may be written as follows

$$\begin{aligned}
&\left[\frac{1}{\mathcal{J}}+\left(\frac{2\Delta t}{3}\right)\delta_{\xi 2}\left(\frac{\partial \boldsymbol{F}^p}{\partial \boldsymbol{Q}}-\frac{1}{Re}\frac{\partial \boldsymbol{F}_v^p}{\partial \boldsymbol{Q}}\right)\right]\mathcal{J}\\
&\quad\times\left[\frac{1}{\mathcal{J}}+\left(\frac{2\Delta t}{3}\right)\delta_{\eta 2}\left(\frac{\partial \boldsymbol{G}^p}{\partial \boldsymbol{Q}}-\frac{1}{Re}\frac{\partial \boldsymbol{G}_v^p}{\partial \boldsymbol{Q}}\right)\right]\mathcal{J}\\
&\quad\times\left[\frac{1}{\mathcal{J}}+\left(\frac{2\Delta t}{3}\right)\delta_{\zeta 2}\left(\frac{\partial \boldsymbol{H}^p}{\partial \boldsymbol{Q}}-\frac{1}{Re}\frac{\partial \boldsymbol{H}_v^p}{\partial \boldsymbol{Q}}\right)\right]\Delta \boldsymbol{Q}\\
&\quad=-\left(\frac{2\Delta t}{3}\right)\left[\left(\frac{1}{2\Delta t}\right)\left(\frac{3\boldsymbol{Q}^p-4\boldsymbol{Q}^n+\boldsymbol{Q}^{n-1}}{\mathcal{J}}\right)\right.\\
&\quad+\delta_{\xi 6}\left(\boldsymbol{F}^p-\frac{1}{Re}\boldsymbol{F}_v^p\right)+\delta_{\eta 6}\left(\boldsymbol{G}^p-\frac{1}{Re}\boldsymbol{G}_v^p\right)\\
&\quad\left.+\delta_{\zeta 6}\left(\boldsymbol{H}^p-\frac{1}{Re}\boldsymbol{H}_v^p\right)-D_c q_c \boldsymbol{S}^p\right] \qquad (12)
\end{aligned}$$

In this expression, which is employed to advance the solution in time, $\boldsymbol{Q}^{p+1}$ is the $p+1$ approximation to $\boldsymbol{Q}$ at the $n+1$ time level $\boldsymbol{Q}^{n+1}$, and $\Delta \boldsymbol{Q}=\boldsymbol{Q}^{p+1}-\boldsymbol{Q}^p$. For $p=1$, $\boldsymbol{Q}^p=\boldsymbol{Q}^n$. Second-order-accurate backward-implicit time differencing was used to obtain temporal derivatives.

The implicit segment of the algorithm incorporates second-order-accurate centered differencing for all spatial derivatives, and uses nonlinear artificial dissipation [43] to augment stability. Efficiency is enhanced by solving this implicit portion of the factorized equations in diagonalized form [44]. Temporal accuracy, which can be degraded by use of the diagonal form, is maintained by using subiterations within a time step. This technique has been commonly invoked in order to reduce errors due to factorization, linearization, diagonalization, and explicit application of boundary conditions. It is useful for achieving temporal accuracy on overset zonal mesh systems and for a domain decomposition implementation on parallel computing platforms. Any deterioration of the solution caused by use of artificial dissipation and by lower-order spatial resolution of implicit operators is also reduced by the procedure. Three subiterations per time step have been applied in the current simulations to preserve second-order temporal accuracy.

The compact difference scheme employed on the right-hand side of Eq. (12) is based upon the pentadiagonal system of Lele [45], and is capable of attaining spectral-like resolution. This is achieved through the use of a centered implicit difference operator with a compact stencil, thereby reducing the associated discretization error. For the present computations, a sixth-order tridiagonal subset of Lele's system is used, which is illustrated here in one spatial dimension as

$$\begin{aligned}
&\alpha\left(\frac{\partial \boldsymbol{F}}{\partial \xi}\right)_{i-1}+\left(\frac{\partial \boldsymbol{F}}{\partial \xi}\right)_i+\alpha\left(\frac{\partial \boldsymbol{F}}{\partial \xi}\right)_{i+1}\\
&\quad=a\left(\frac{\boldsymbol{F}_{i+1}-\boldsymbol{F}_{i-1}}{2}\right)+b\left(\frac{\boldsymbol{F}_{i+2}-\boldsymbol{F}_{i-2}}{4}\right) \qquad (13)
\end{aligned}$$

with $\alpha=1/3$, $a=14/9$, and $b=1/9$. The scheme has been adapted by Visbal and Gaitonde [46] as an implicit, iterative time-marching technique, applicable for unsteady vortical flows. It is used in conjunction with a tenth-order low-pass Pade-type nondispersive spatial filter developed by Gaitonde et al. [47], which has been shown to be superior to the use of explicitly added artificial dissipation for maintaining both stability and accuracy on stretched curvilinear meshes [46]. The filter is applied to the solution vector sequentially in each of the three computational directions following each subiteration, and is implemented in one dimension as

$$\alpha_f \hat{\boldsymbol{Q}}_{i-1}+\hat{\boldsymbol{Q}}_i+\alpha_f \hat{\boldsymbol{Q}}_{i+1}=\sum_{n=0}^{5}\frac{a_n}{2}\left(\boldsymbol{Q}_{i+n}+\boldsymbol{Q}_{i-n}\right) \qquad (14)$$

where $\hat{\boldsymbol{Q}}$ designates the filtered value of $\boldsymbol{Q}$. It is noted that the filtering operation is a postprocessing technique, applied to the evolving solution in order to regularize features that are captured but poorly resolved. Equation (14) represents a one-parameter family of tenth-order filters, where numerical values for the a_ns may be found in [48]. The filter coefficient α_f is a free adjustable parameter that may be selected for specific applications, and has been set to 0.40 for the present simulations.

The aforementioned features of the numerical algorithm are embodied in a parallel version of the time-accurate three-dimensional computer code FDL3DI [48], which has proven to be reliable for steady and unsteady fluid flow problems, including vortex breakdown [49,50], transitional wall jets [51], synthetic jet actuators [52], roughness elements [53], plasma flows [37–40], and direct numerical and large eddy simulations of subsonic [23,54] and supersonic flowfields [55,56].

V. LES Approach

In a traditional LES approach, physical dissipation at the Kolmogorov scale is not represented. For spatially nondissipative numerical schemes, without use of SGS models, this leads to an accumulation of energy at high mesh wave numbers and ultimately to numerical instability. Explicitly added SGS models are then employed as a means to dissipate this energy. In the present methodology, the effect of the smallest fluid structures is accounted for by an implicit large eddy simulation (ILES) technique, which has been successfully used for a number of turbulent and transitional computations. The ILES approach was first introduced by Visbal et al. [57,58] as a formal alternative to conventional methodologies and is predicated upon the high-order compact differencing and low-pass spatial filtering schemes, without the inclusion of additional SGS modeling. This technique is similar to monotonically integrated large eddy simulation (MILES) [59] in that it relies upon the numerical solving procedure to provide the dissipation that is typically supplied by traditional SGS models. Unlike MILES, however, dissipation is contributed by the aforementioned high-order Pade-type low-pass filter only at high spatial wave numbers where the solution is poorly resolved. This allows a mechanism for the turbulence energy to be dissipated at scales that cannot be accurately resolved on a given mesh system, in a fashion similar to subgrid modeling. For purely laminar flows, filtering may be

required to maintain numerical stability and preclude a transfer of energy to high-frequency spatial modes due to spurious numerical events. The ILES methodology thereby permits a seamless transition from large eddy simulation to direct numerical simulation as the resolution is increased. In the ILES approach, the unfiltered governing equations may be employed, and the computational expense of evaluating subgrid models, which can be substantial, is avoided. This procedure also enables the unified simulation of flowfields where laminar, transitional, and turbulent regions simultaneously coexist.

It should also be noted that the ILES technique may be interpreted as an approximate deconvolution SGS model [60], which is based upon a truncated series expansion of the inverse filter operator for the unfiltered flowfield equations. Mathew et al. [61] have shown that filtering provides a mathematically consistent approximation of unresolved terms arising from any type of nonlinearity. Filtering regularizes the solution and generates virtual subgrid model terms that are equivalent to those of approximate deconvolution.

VI. Details of the Computations

A. Computational Meshes

The computational mesh system surrounding the baseline cylinder case consisted of three distinct geometric regions, which appear in Fig. 3a and 3b. The origin of the system in Fig. 3a is located at the inboard centerline of the cylinder, but for clarity it is shown at the outboard boundary in the figure. Each of the regions comprises planar grids that were uniformly distributed in the spanwise direction. The spanwise extent of the domain is πD and is described by 197 of the planar grids.

An O-grid topology was used to define the near-surface flowfield, using a mesh of (255×171) points in the circumferential and radial directions, respectively. The grid extends a distance of one diameter from the surface and has a uniform nondimensional radial spacing of 0.00025 at the wall. A five-grid-point overlap of the mesh was constructed upstream of the cylinder leading edge in order to enforce circumferential periodicity. Downstream of the near surface region, a rectangular grid employing (355×141) points in the x and y directions was used to capture the cylinder wake flow. The streamwise distribution in this region was uniform up to $x = 5.0$ and then was stretched to the downstream boundary, which was located at $x = 100$. In the uniform region, $\Delta x = \Delta y = 0.02$. A C-grid topology was employed to connect the near-cylinder and wake regions to the outer boundary, which was located $100D$ from the cylinder axis and wake centerline. The far-field boundary can be observed in Fig. 3b. The C-grid mesh consisted of 295 points in the circumferential direction, and 81 points normal to the near-cylinder and wake grids. For one of the control cases to be described subsequently, a locally refined mesh was used in the near-wall region, as is seen in Fig. 3c. For this case, the outer O-grid consisted of (255×89) points, whereas the refined region was composed of (787×89) points that were distributed nonuniformly in the circumferential direction. These grid systems resulted in flowfields that were described by 34.0×10^6 total points when the locally refined mesh was employed and 23.6×10^6 points for all other cases.

Flow variables in regions of overlapped meshes were transferred between the grids via explicit sixth-order accurate Lagrangian interpolation formulae. This interpolation approach for high-order numerical solutions has been successfully applied by Sherer and Visbal [62,63] for acoustic problems and large eddy simulations using overset grids, and by Rizzetta and Visbal [64,65] for direct numerical simulations and flow-control applications.

In addition to the meshes defined here, a coarse-grid system was constructed by removing every other point in each coordinate direction. The coarsened system was used to provide a resolution study for the baseline flow without actuation and to perform preliminary explorations of control strategies.

B. Boundary Conditions

Along the circumferential outer boundary of the C-grid domain, freestream conditions were specified for all flow variables. Downstream, the exit static pressure (p_∞) was fixed, and other flow variables were extrapolated from within the interior domain. The downstream domain was intensionally severely stretched in the streamwise direction to prevent spurious reflections from the outflow boundary. This technique transfers information to high spatial wave numbers and then dissipates it by the low-pass filter [66].

On the cylinder surface, the no-slip condition was enforced along with an isothermal wall, and a fourth-order accurate representation of the zero-normal pressure gradient. Periodic conditions were applied at the spanwise domain boundaries. This was facilitated by using a 5-plane overlap at $z = 0$ and $z = \pi$, so that a total of 201 grid points were employed in the spanwise direction.

C. Temporal Considerations

Operationally, DBD actuators are inherently unsteady devices. As mentioned previously, within the context of the empirical model, however, the body force imposed on the fluid is assumed to be steady owing to the high frequency of the applied voltage. These devices may also be operated in a pulsed manner as described by Corke and Post [67], thereby reducing total power consumption. The pulsed mode of operation also introduces low-frequency forcing to the flow, which may be more receptive to control, and offers the potential of improved effectiveness. For simulation of pulsed actuation, the forcing amplitude is modulated according to the duty cycle illustrated in Fig. 4. Here, t_d is the portion of the fundamental period t_p over which the device is active. The ratio $t_d/t_p \times 100$ expressed as

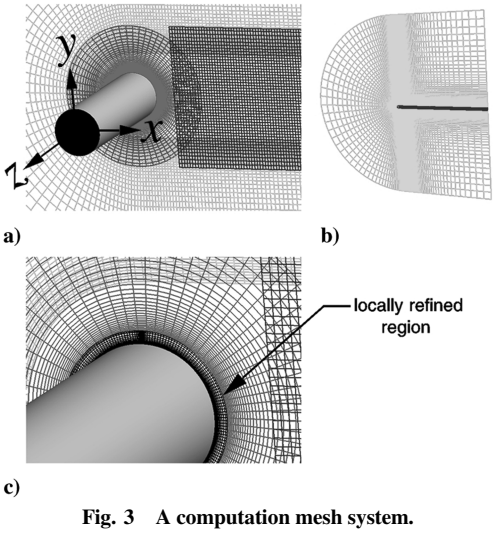

Fig. 3 A computation mesh system.

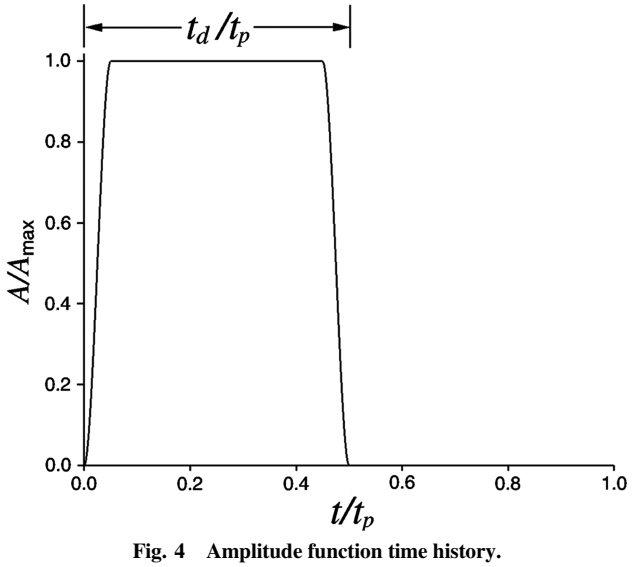

Fig. 4 Amplitude function time history.

a percentage is commonly referred to as the duty cycle, which is 50% in the present case. The amplitude time history for one cycle appearing in the figure consists of a series of piecewise continuous cubic and linear functions, which were used to represent the pulsing duration. The amplitude function was then appended as a factor to the plasma-force magnitude in order to establish pulsed control. This description is identical to that used in previous flow-control simulations [65,68]. It should be noted that the applied waveform introduces multiple harmonics of the primary frequency, as was demonstrated in [39,69]. The nondimensional forcing frequency $\mathcal{F}$ was chosen as 1.25, where

$$\mathcal{F} = Df/u_\infty \tag{15}$$

Apart from one solution that was generated to study temporal resolution, all the computations presented here were obtained using a time step of $\Delta t = 5.0 \times 10^{-4}$, where t is nondimensionalized by reference quantities. For this value, the duty cycle displayed in Fig. 4 was described by 1600 time steps. Flowfields for each case were initialized from previously obtained solutions, and processed for 100,000 time steps in order to remove transients and attain an equilibrium state. Final results were then evolved for at least an additional 200,000 time steps during which statistical information was collected. Statistics were monitored to assure that a converged sample was achieved. This duration represents approximately 20 cylinder vortex-shedding cycles, and 125 actuation cycles of the pulsed control.

D. Actuator Configurations

The cylinder configurations of the baseline and control situations are found in Fig. 5. Two different arrangements of actuators were considered in this investigation. The first of these employed actuators located at the top and bottom of the cylinder ($\theta = 90, 270$ deg), which extended 30 deg circumferentially along the surface. The nondimensional arc length along the surface ($0.5\Delta\theta$, θ in radians) here corresponds to the actuator length AC in Fig. 2. These actuators produced a plasma-force vector with components directed streamwise in the flow direction and toward the solid surface, resulting in a wall-jet-like flow along the cylinder. The wall jet created a Coanda flow, thus delaying separation and reducing the effect of shedding vortical structures. Both continuous (case C) pulsed actuation (cases CPI, CPO) were simulated for this arrangement. With pulsed actuation, the top and bottom actuators could be operated independently. Solutions were obtained with pulsing cycles that were synchronized (case CPI) and also that were 180 deg out of phase (case CPO). The second arrangement consisted of very small pulsed actuators located at the top and bottom of the cylinder (case S), which manipulated the unstable shear layer near the separation point, in order to exert control. We note that case C was similar to the configuration considered by Thomas et al. [32,33] for cylinders at higher Reynolds numbers.

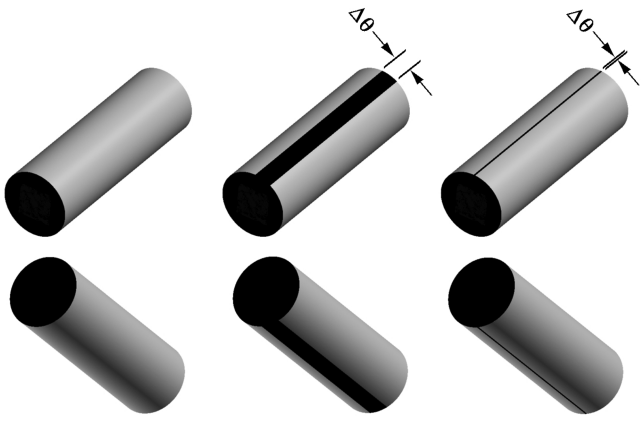

Fig. 5 Cylinder actuator configurations.

The electric field of the empirical plasma model, shown schematically in the Cartesian system of Fig. 2, is represented in cylindrical coordinates for the present application. The maximum nondimensional extent of the field from the cylinder surface was taken as 0.0125, which corresponds to BC in Fig. 2. This value is approximately one half of the boundary layer thickness in the region of attached flow upstream of the separation point. The circumferential extents of the electric field are specified as $\Delta\theta = 30$ deg for cases C, CPI, and CPO, and $\Delta\theta = 2.825$ deg for case S. The arclengths of these extents correspond to AC in Fig. 2.

E. Domain Decomposition

For parallel processing, the previously described computational domains were decomposed into a series of subzones, which were then distributed on individual processors of a massively parallel computing platform. Decompositions were constructed to provide an approximately equal number of grid points in every subzone, thereby balancing the computational work load among the processors. Faces at the boundaries of each subzone block were overset into adjacent domains, such that an overlap of five planes was established. Although this incurred an overhead due to redundant computation, it maintained the formal high-order accuracy of both the numerical differencing and filtering schemes. Because a vast majority of the overlapping mesh points of the respective decompositions were coincident, no further interpolation was required. Automated software [70] was used to identify donor and recipient grid points in the overlapping domains. Internode communication among the processors was established through standard message-passing interface (MPI) library routines [71], which were used to transfer information between the various subzones of the flowfield at domain boundaries. A total of 288 processors were employed for computations using the three-block mesh system shown in Fig. 3a (cases B, C, CPI, and CPO), and 368 processors used when the four-block system of Fig. 3c was required (case S).

VII. Baseline Case

Features of the baseline cylinder flow without control are found in Figs. 6–11. Given in Table 1 are quantities of interest for all simulations, which can be used to compare the control cases with each other and with the baseline flow. Also included in the table are results from Dong et al. [27], which solved an incompressible formulation of the governing equations using a spectral element method. For the baseline case, the time-mean lift coefficient $\bar{C}_l$ provides an indication of convergence of the temporal average. The baseline case appeared to be characterized by a low-frequency wake mode. Because of this, time-mean quantities were based upon a temporal sample of 500,000 time steps. In control situations, vortex shedding and wake unsteadiness was reduced, and so an extended sample for time averaging was not necessary.

A. Time-Mean Flowfield

Time-mean surface pressure coefficient distributions are presented in Fig. 6. These results have been averaged both temporally and in the spanwise direction. It should also be noted that for all of the results appearing in Figs. 6, 7, and 10, averaging was also performed about the cylinder vertical midplane ($y = 0.0$). This was done in order to achieve a long-time statistical representation with a minimum expenditure of computational resources. Seen in the figure are simulations performed on both the standard and coarse computational mesh systems. Because there are no experimental measurements at the given flow conditions ($Re = 10,000$), data are displayed for $Re = 3900$ from [20] and for $Re = 8000$ from [3]. The figure indicates that the coarse-grid result is not sufficiently fine to obtain the proper pressure distribution. It should be remembered that the coarse-mesh system contains just one-eighth the number of grid points as that of the finer mesh and is only used to provide some indication of spatial resolution.

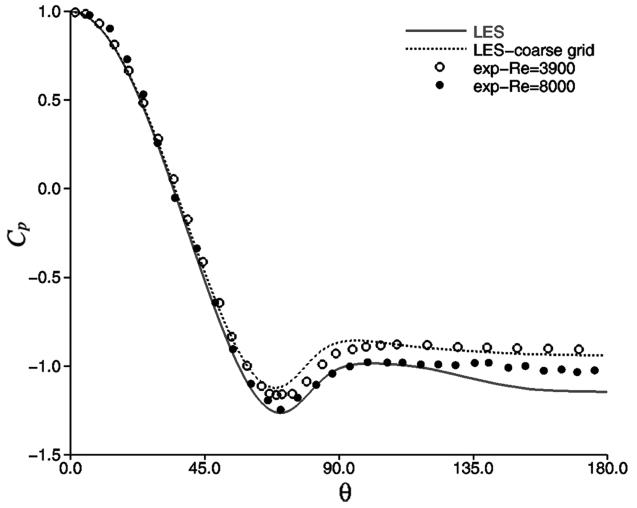

Fig. 6 Time-mean surface pressure distributions for the baseline case B.

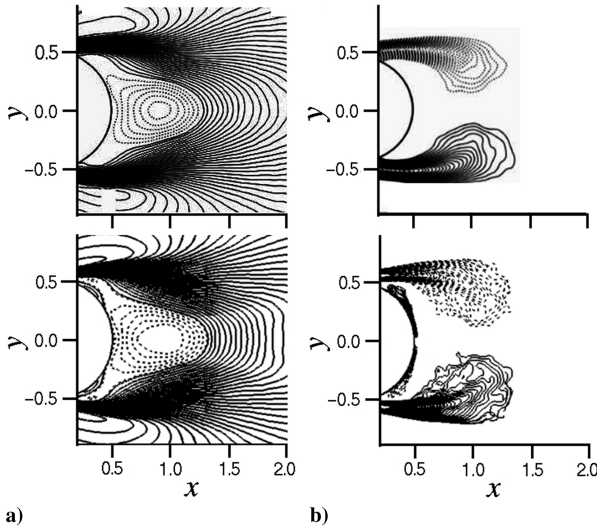

Fig. 7 Time-mean contours for the baseline case B showing a) u velocity, and b) spanwise vorticity, of the experiment (upper) and the LES (lower).

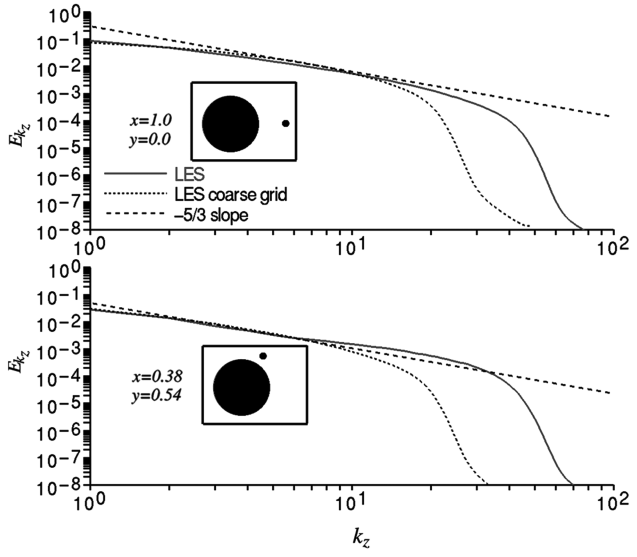

Fig. 8 Time-mean turbulent kinetic energy spanwise wave-number spectra for the baseline case B.

Time-mean planar contours of the streamwise velocity component u and the spanwise vorticity are compared with the experiment of Ekmekci [7] in Fig. 7. The contour levels in the figure are identical to those of [7,27]. The extent of the separation bubble for the present computation seems to agree reasonably well with the experiment.

Time-mean turbulent kinetic energy spanwise wave-number spectra are observed in Fig. 8 at two different locations in the flowfield. Wave-number spectra were generated for each time step, and then temporally averaged to produce results in the figure. One of the positions is on the wake centerline ($x = 1.0$, $y = 0.0$), whereas the other lies in the region of the unstable shear layer ($x = 0.38$, $y = 0.54$). Solutions on the standard and coarse computational meshes are represented in the figure. Spectra at both locations contain long extents in wave-number space within the inertial range. This is an indication of adequate resolution in the spanwise direction. Apart from a lack of the ability to represent the energy at higher wave numbers correctly, it is considered significant that the coarse-grid result compares well with its more refined counterpart.

B. Instantaneous Flowfield

Shown in Fig. 9 are time histories of the integrated cylinder lift and drag coefficients. The irregular patterns in these distributions emphasize the difficulty in collecting long-time statistical samples. Time-mean planar contours of the fluctuating streamwise velocity component (u'_{rms}) and the Reynolds stress ($\overline{u'v'}$) are compared with the experiment of Ekmekci [7] in Fig. 10. As in Fig. 7, the contour levels are the same as those in [7,27]. Although the respective comparisons are qualitatively similar, some specific details differ.

Turbulent kinetic energy frequency spectra are observed in Fig. 11. Locations in this figure are the same as those of the spatial wave-number spectra in Fig. 8. Results in the figure were constructed by generating spectra at all spanwise locations and then spatially averaging these in the spanwise direction. Found in the figure are spectra arising from simulations using two different time-step sizes. Spectra at both locations illustrate the fundamental vortex shedding frequency with a Strouhal number $St \approx 0.2$ (see Table 1), and its first harmonic. Instabilities in the shear layer are not detected in the spectra of the wake midplane ($x = 1.0$, $y = 0.0$). The frequency of the shear-layer instability lies in a band centered at approximately 15 times that of the fundamental, which is consistent with the direct numerical simulation of Dong et al. [27]. The smaller time-step solution gives slightly higher energy levels, presumably due to better temporal resolution of fluctuating quantities. The fact that the larger time-step result produces the same frequency peaks as that of the small time-step solution supplies some level of confidence to the simulations in general. Because statistics with the small time step were collected for only 150,000 time steps (as opposed to 500,000), spectral features are sharper for the large time-step result.

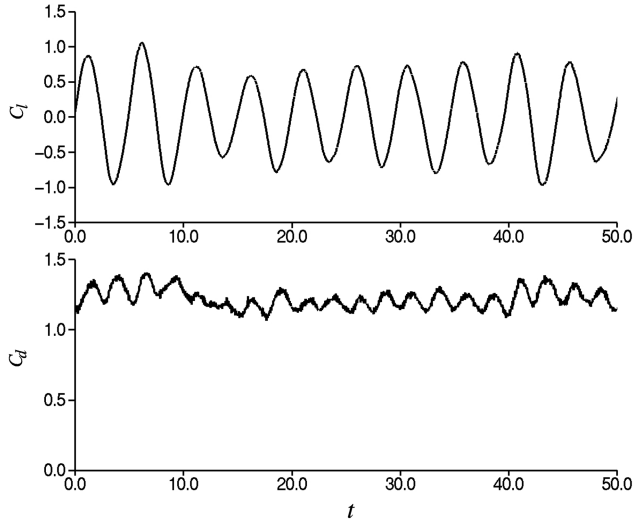

Fig. 9 Time history of the cylinder lift (upper) and drag (lower) coefficients for the baseline case B.

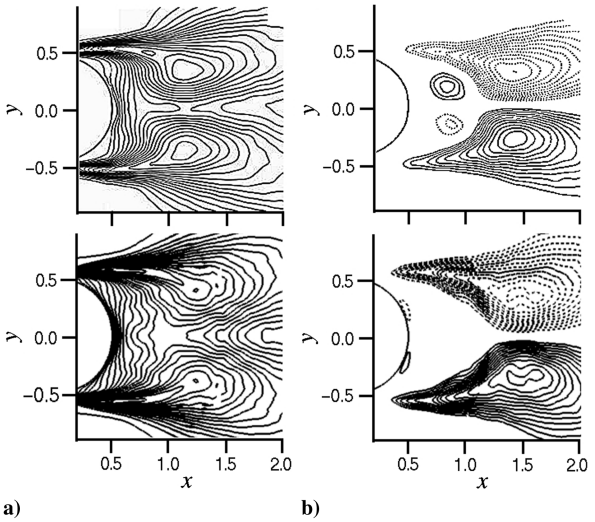

Fig. 10 Time-mean contours for the baseline case B showing a) u'_{rms}, and b) $\overline{u'v'}$, of the experiment (upper) and the LES (lower).

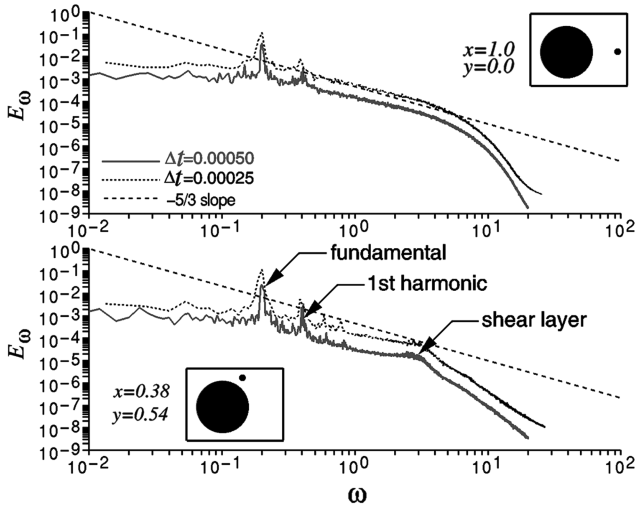

Fig. 11 Turbulent kinetic energy frequency spectra for the baseline case B.

VIII. Control Cases

For the control cases producing Coanda flow (C, CPI, CPO), D_c was prescribed as 50.0. This value was derived from preliminary coarse-grid simulations and corresponds approximately to the least amount of plasma actuation required to exert effective control. In the shear-layer manipulation case (S), D_c had to be increased to 100.0 due to the limited extent of the actuator electric field. Without this increase, only minimal control was exerted. Pulsed actuation was employed for cases CPI, CPO, and S, using the 50% duty cycle demonstrated in Fig. 4 to lower the total power requirements. The forcing frequency in these cases $\mathcal{F} = 1.25$, was taken as approximately one half that of the natural shear-layer frequency of the baseline case B. This choice was motivated by the experimental investigation of Chyu and Rockwell [14] for oscillating control of cylinders at low Reynolds numbers, who determined that excitation was most effective when applied at subharmonics of the shear-layer frequency. It was found in the present investigation that pulsed plasma actuation imposed at a higher frequency ($\mathcal{F} = 4.0$) established no effective control.

As previously noted, Table 1 provides a number of quantities by which to compare the respective simulations. Single actuator energy requirements may be estimated by the integrated power-per-unit span generated by the electric field arising from the empirical plasma model. This power usage is given by

$$\left[\frac{\rho_\infty u_\infty^3 D_c}{D}\right] P_i \tag{16}$$

where

$$P_i = \frac{1}{t_p}\int_0^{t_p}\iint A(t)|\boldsymbol{E}(r,\theta)|r\mathrm{d}r\mathrm{d}\theta\mathrm{d}t \tag{17}$$

In the preceding expression, the region in r, θ corresponds to the extent of the electric field, shown schematically for the Cartesian system in Fig. 2. For pulsed actuation, $A(t)$ is given by the amplitude function illustrated in Fig. 4 and in the continuous case $A(t) \equiv 1.0$.

In the unsteady Coanda flow-control case CPI, actuators on the top and bottom of the cylinder were pulsed in phase with each other. The initial condition of the flowfield was established as the equilibrium state for the continuous case C. It was expected that the pulsed case would attain an equilibrium condition with a time-mean flow that had zero lift. On the contrary, case CPI produced a time-mean flowfield with negative lift. It was thought that no stable flowfield with time-mean zero lift was possible for the pulsed case, but it was believed that both negative and positive lift situations could be achieved. Unsteady Coanda flow control was also investigated, where the top and bottom actuators were pulsed 180 deg out of phase from each other (case CPO). This case was also initialized from the continuous case C. Actuation was begun by having the top actuator active and the bottom actuator inactive. This procedure resulted in positive lift immediately following the onset of actuation, in the hope that a time-mean flowfield with positive lift would result. This was in fact the case. Thus the time-mean flows for Coanda control, which were pulsed in phase and out of phase, appeared to be mirror reflections of each other about the wake centerline ($y = 0$).

Apparently, there is no stable time-mean symmetric solution for the configuration considered, and the bistable positive or negative lift states are a function of the initial conditions. This is probably not surprising, considering the complexity of the highly nonlinear transitional near-wake flow. The instantaneous flowfield is never symmetric about the wake centerline, so that at any point in time, vortical shedding at the top and bottom of the cylinder are in different stages of development. When actuation is initiated, the body force can shift the shedding dynamics to a new configuration. Because of the initial position and strength of the respective vortices, there is no reason to assume that the new shedding should remain symmetric about the centerline. The new equilibrium dynamics will be dictated by the initial state of the flow when actuation is commenced, as well

Table 1 Summary of cylinder computational results

Case	Control	D_c	Designation	$\bar{C}_l$	$\bar{C}_d$	$\bar{C}_{pB}$	$C_{l\mathrm{rms}}$	St	P_i
Baseline	NA	NA	B	0.002	1.214	−1.145	0.550	0.204	NA
Baseline coarse grid	NA	NA	NA	0.003	1.115	−0.962	0.417	0.196	NA
Baseline $\Delta t = 0.00025$	NA	NA	NA	0.000	1.261	−1.425	0.646	0.200	NA
Baseline [27]	NA	NA	NA	NA	1.143	−1.129	0.448	0.203	NA
Coanda	Continuous	50.0	C	0.004	0.342	−0.297	0.024	NA	3.453×10^{-3}
Coanda	Pulsed in phase	50.0	CPI	−0.631	0.329	−0.128	0.033	NA	1.726×10^{-3}
Coanda	Pulsed out of phase	50.0	CPO	0.607	0.328	−0.118	0.051	NA	1.726×10^{-3}
Shear layer	Pulsed in phase	100.0	S	0.002	0.574	−0.465	0.032	NA	3.297×10^{-4}

as the manner in which pulsing is begun (i.e., which actuator is started first when pulsing out of phase).

A. Time-Mean Flowfields

Presented in Fig. 12 are time-mean surface pressure coefficient distributions for all four control cases. For this figure, and others to follow (Figs. 16–18 and 21), symbols on the respective curves are used only to differentiate one result from another and do not represent only isolated locations where the solutions are available. The baseline result has also been provided for comparison. As seen in the figure, cases B, C, and S all have distributions, which are symmetric about the top and bottom cylinder surfaces. The pulsed Coanda cases CPI and CPO are asymmetric, and, as noted previously, the two results are mirror images of each other. Figure 13 exhibits time-mean planar contours of the u velocity component. These contours, and other time-mean results to follow, have been averaged in the spanwise direction as well as temporally. Wakes for the Coanda cases C, CPI, and CPO appear to be the smallest.

Appearing in Fig. 14 are streamline patterns of the time-mean flowfields. The recirculating flow in the cylinder base regions are clearly visible, indicating a very long extent for the shear-layer control case (S) and much shorter zones for Coanda control. All of the control cases appreciably reduced the cylinder mean drag (see Table 1), which was attributed to a modification of the base pressure, so that the extent of recirculation was not directly a measure of control effectiveness. Corresponding time-mean contours of the spanwise vorticity are displayed in Fig. 15. Here, expansion of the wake in the vertical direction for the baseline flow, relative to the control cases, is evident.

Shown in Fig. 16 are time-mean turbulent kinetic energy spanwise wave-number spectra. In the cylinder wake ($x = 1.0$, $y = 0.0$), spectra for the control cases are observed to be similar to the baseline, and all evidence an appreciable inertial range. This is not true for the spectra obtained at a point just above the cylinder ($x = 0.38$, $y = 0.54$). For the baseline case, this point was located within the unstable shear layer, contributing to the roll up of shed vortices. Because of the wall-jet-like flow created in the Coanda control cases, the shear layer no longer traverses this location. With shear-layer control, the spectra is similar to the baseline case.

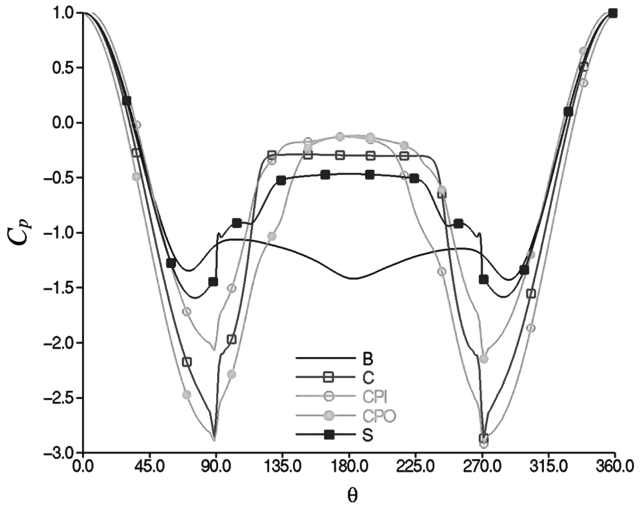

Fig. 12 Time-mean surface pressure distributions for the control cases.

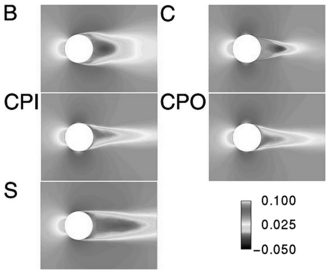

Fig. 13 Time-mean planar contours of u velocity for the control cases.

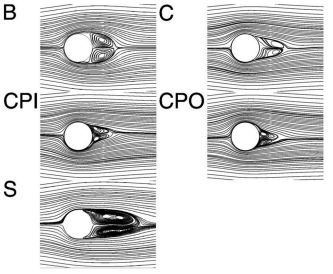

Fig. 14 Time-mean streamlines for the control cases.

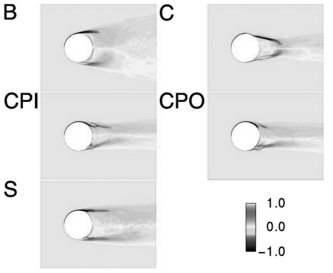

Fig. 15 Time-mean planar contours of spanwise vorticity for the control cases.

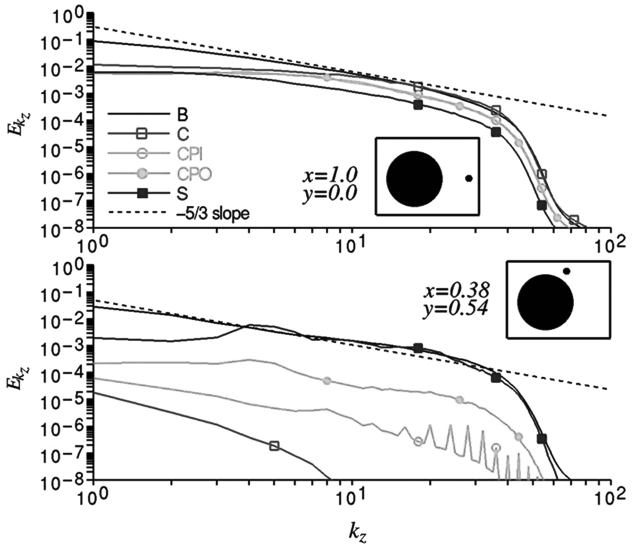

Fig. 16 Time-mean turbulent kinetic energy spanwise wave-number spectra for the control cases.

B. Instantaneous Flowfields

Time histories of the integrated lift coefficients are displayed in Fig. 17. All of the control cases have essentially removed lift unsteadiness (see $C_{l\text{rms}}$ in Table 1). This was brought about because shedding of large-scale vortical structures has been reduced or eliminated. Corresponding histories of the drag coefficients are given in Fig. 18. Time-mean values of drag have been decreased by more than 70% for all of the Coanda cases (C, CPI, CPO), and by more than 50% for the shear-layer control (S). It should be noted that the power requirement for the shear-layer case is substantially lower than that of the Coanda cases (see P_i in Table 1). Also, for the pulsed Coanda cases (CPI and CPO), although the mean drag has been decreased,

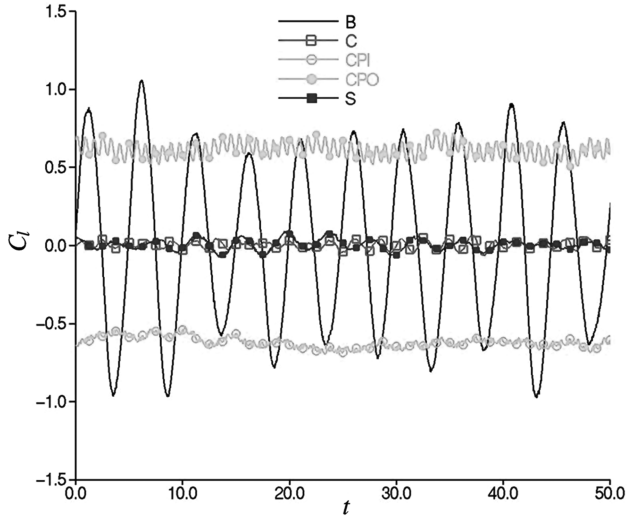

Fig. 17 Time history of the cylinder lift coefficient for the control cases.

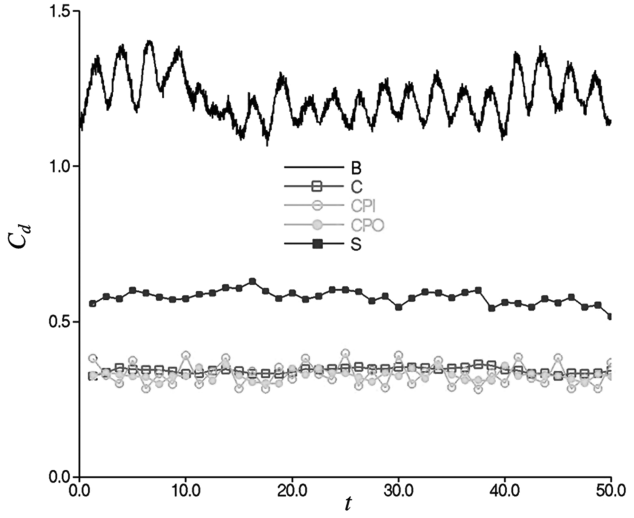

Fig. 18 Time history of the cylinder drag coefficient for the control cases.

there is a nonzero mean lift contributing an average force acting on the cylinder.

Instantaneous planar contours of the u velocity component at the midspan location are found in Fig. 19. Features of the unsteady wake are visible in the figure, where dark contours indicate the low-speed region. Corresponding contours of the spanwise component of vorticity in Fig. 20 illustrate fine-scale fluid structures. Small vortical structures evolving from the shear-layer near separation may be observed in the flowfields of the pulsed cases (CPI, CPO, and S). For the continuous actuation Coanda case (C), the shear layer has been regularized by the wall-jet flow.

Presented in Fig. 21 are turbulent kinetic energy frequency spectra for the control cases. Spectra taken in the cylinder wake region ($x = 1.0$, $y = 0.0$) do not exhibit peaks associated with a fundamental shedding frequency, as seen with the baseline case. Also at this location, the control cases exhibit a less substantial inertial range. Virtually no inertial range appears in the spectra at the location that characterized the shear-layer for the baseline case ($x = 0.38$, $y = 0.54$). Here, for the pulsing cases, harmonics of the forcing frequency are apparent in the spectra. Higher harmonics are naturally excited by the step-function-like character of the amplitude function A (see Fig. 4). Subharmonics are generated by the vortex formation process in the unstable shear layer and have been previously observed in plasma-base control for low-pressure turbine blades [65]. In case CPO, the out-of-phase pulsing of actuators also

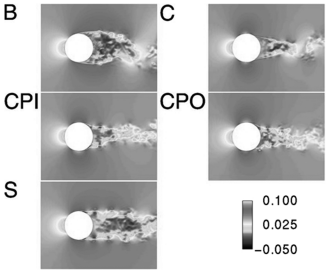

Fig. 19 Instantaneous planar contours of u velocity for the control cases.

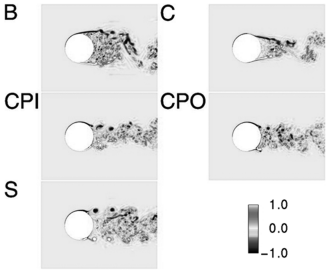

Fig. 20 Instantaneous planar contours of spanwise vorticity for the control cases.

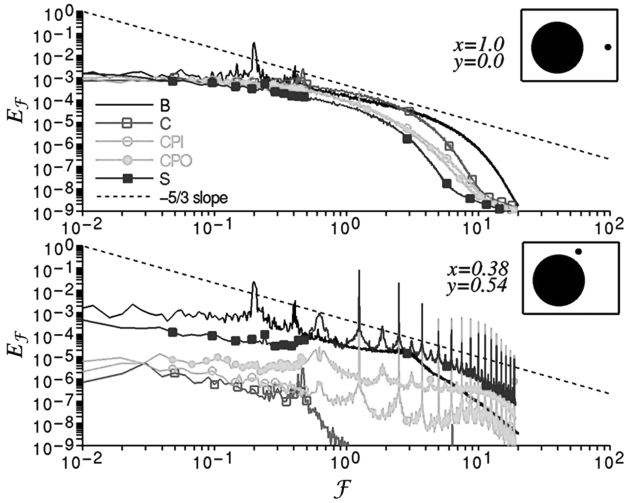

Fig. 21 Turbulent kinetic energy frequency spectra for the control cases.

produces a subharmonic of the fundamental frequency. At the shear-layer location, little inertial region is evident for any of the control cases.

Three-dimensional representations of the cylinder flowfields are provided in Fig. 22 by isosurfaces of the vorticity magnitude, which have been colored by u velocity. The value of the vorticity magnitude in the isosurfaces corresponds to that at the edge of the boundary layer in the flow upstream of separation. Fine-scale structures, which have been captured by the high-order solutions, are evident in the figure. Massive roll up of the primary vortex is obvious in the baseline case B. With continuous Coanda control (C), the virtual wall jets generated by plasma actuation have cut off large vortical shedding immediately behind the cylinder. The shear layers can been seen rolling up further downstream in the wake for this situation. When pulsing is employed in the Coanda control (CPI and CPO), the full span actuators produce coherent vortical structures, which are generated by a roll up of the shear layers. These bring high momentum fluid from the outer flow region into the unsteady wake and help preclude massive shedding. A similar situation occurs for

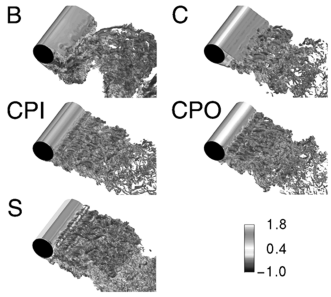

Fig. 22 Instantaneous isosurfaces of vorticity magnitude colored by *u* velocity for the control cases.

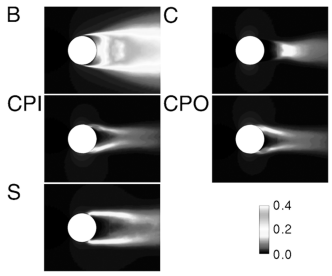

Fig. 23 Time-mean planar contours of turbulent kinetic energy for the control cases.

the shear-layer control case (S), but here the long vortical structures are initiated closer to the top and bottom of the cylinder in proximity to the actuator locations. This is brought about by manipulation of the shear layer near separation, as no wall jet is present.

Time-mean turbulent kinetic energy contours are displayed in Fig. 23. The figure illustrates that all of the control cases have dramatically reduced the large velocity fluctuations that were present in the baseline flow. As can be seen in the figure, a large amount of energy is present in the near wake for the baseline case. In control situations, small amounts of turbulent energy reside primarily in the shear layers.

IX. Conclusions

An implicit large eddy simulation technique was used to explore plasma-based control strategies for flow about a circular cylinder at a Reynolds number of 10,000. A high-order numerical method with an overset grid approach captured fine-scale fluid structures in the transitional and near-wake regions. For the baseline case without control, the simulation was found to agree reasonably well with available experimental data. A phenomenological model was used to represent the body forces induced by actuators on the surrounding fluid. This simplified approach allowed the investigation of complex flow situations, without incurring the additional computational overhead associated with more sophisticated physical descriptions. Two separate strategies were considered in the investigation, consisting of Coanda flow control and shear-layer manipulation.

All of the control cases were effective in reducing the cylinder unsteady lift and mean drag coefficients. A reduction in mean drag by 70% was achieved by Coanda actuation and by 50% for the shear-layer control. Oscillating lift components were virtually eliminated in all situations. It should be mentioned that in all control cases, large-scale unsteadiness eventually evolved in the wake, at a distance of several diameters downstream of the cylinder. This was promoted by the unstable shear layers, which have a natural predisposition to roll up. The amplitude of the wake oscillation, however, was considerably reduced from those in the baseline case. A bistable state was identified for pulsed Coanda control, which led to nonzero time-mean lift. Pulsed actuation with a 50% duty was found to be as effective as continuous control but reduced the overall power requirements. In this regard, shear-layer control had the smallest power utilization and was only slightly less effective than other strategies.

These simulations compliment previous experimental investigations of plasma-based actuation for bluff body flows. They evidence the potential of plasma actuators for reducing forces acting on these bodies and eliminating massive unsteadiness. Such control may be useful for increasing efficiency, reducing adverse aeroelastic effects, prolonging fatigue life, and decreasing acoustic noise in practical applications.

Acknowledgments

The work presented here was sponsored by the U.S. Air Force Office of Scientific Research and was monitored by R. W. Jefferies and J. D. Schmisseur. Computational resources were supported in part by a grant of supercomputer time from the U.S. Department of Defense Major Shared Resource Center at Wright–Patterson Air Force Base, Ohio.

References

[1] Unal, M. F., and Rockwell, D., "On Vortex Formation from a Cylinder. Part 1. The Initial Instability," *Journal of Fluid Mechanics*, Vol. 190, May 1988, pp. 491–512. doi:10.1017/S0022112088001429

[2] Szepessy, S, and Bearman, P. W., "Aspect Ratio and End Plate Effects on Vortex Sheedung from a Circular Cylinder," *Journal of Fluid Mechanics*, Vol. 234, Jan. 1992, pp. 191–217. doi:10.1017/S0022112092000752

[3] Norberg, C., "An Experimental Investigation of the Flow Around a Circular Cylinder: Influence of Aspect Ratio," *Journal of Fluid Mechanics*, Vol. 258, Jan. 1994, pp. 287–316. doi:10.1017/S0022112094003332

[4] Lin, J.-C., Towfighi, J., and Rockwell, D., "Instantaneous Structure of the Near-Wake of a Circular Cylinder: On the Effect of Reynolds Number," *Journal of Fluids and Structures*, Vol. 9, No. 4, May 1995, pp. 409–418. doi:10.1006/jfls.1995.1023

[5] Williamson, C. H. K., "Vortex Dynamics in the Cylinder Wake," *Annual Review of Fluid Mechanics*, Vol. 28, Jan. 1996, pp. 477–539. doi:10.1146/annurev.fl.28.010196.002401

[6] Norberg, C., "Fluctuating Lift on a Circular Cylinder: Review and New Measurements," *Journal of Fluids and Structures*, Vol. 17, No. 1, Jan. 2003, pp. 57–96. doi:10.1016/S0889-9746(02)00099-3

[7] Ekmekci, A., "Control of the Near-Wake of a Circular Cylinder: Effects of Surface Disturbances," Ph.D. Thesis, Lehigh Univ., 2006.

[8] Bloor, M. S., "The Transition to Turbulence in the Wake of a Circular Cylinder," *Journal of Fluid Mechanics*, Vol. 19, June 1964, pp. 290–304. doi:10.1017/S0022112064000726

[9] Gerrard, J. H., "Experimental Investigation of Separated Boundary Undergoing Transition to Turbulence," *Physics of Fluids*, Vol. 10, No. 9, Sept. 1967, pp. S98–S100. doi:10.1063/1.1762514

[10] Gerrard, J. H., "The Wakes of Cylindrical Bluff Bodies at Low Reynolds Number," *Philosophical Transactions of the Royal Society of London. Series A, Mathematical and Physical Sciences*, Vol. 288, No. 1354, March 1978, pp. 351–382. doi:10.1098/rsta.1978.0020

[11] Wei, T., and Smith, C. R., "Secondary Vortices in the Wake of Circular Cylinders," *Journal of Fluid Mechanics*, Vol. 169, Aug. 1986, pp. 513–533. doi:10.1017/S0022112086000733

[12] Filler, J. R., Marston, P. L., and Mih, W. C., "Response of the Shear Layers Separating from a Circular Cylinder to Small-Amplitude Rotational Oscillations," *Journal of Fluid Mechanics*, Vol. 231, Oct. 1991, pp. 481–499. doi:10.1017/S0022112091003476

[13] Roshko, A., "Perspectives on Bluff Body Aerodynamics," *Journal of Wind Engineering and Industrial Aerodynamics*, Vol. 49, No. 1, Dec. 1993, pp. 79–100. doi:10.1016/0167-6105(93)90007-B

[14] Chyu, C. K., and Rockwell, D., "Near-Wake Structure of an Oscillating Cylinder: Effect of Controlled Shear-Layer Vortices," *Journal of Fluid Mechanics*, Vol. 322, Sept. 1996, pp. 21–49. doi:10.1017/S0022112096002698

[15] Prasad, A., and Williamson, C. H. K., "The Instability of the Shear Layer Separating from a Bluff Body," *Journal of Fluid Mechanics*, Vol. 333, Feb. 1997, pp. 375–402. doi:10.1017/S0022112096004326

[16] Brede, M., "Measurements of Turbulence Production in the Cylinder Separated Shear-Layer Using Event-Triggered Laser-Doppler Anemometry," *Experiments in Fluids*, Vol. 36, No. 6, June 2004, pp. 860–866. doi:10.1007/s00348-003-0768-9

[17] Beaudan, P., and Moin, P., "Numerical Experiments on the Flow Past a Circular Cylinder at Subcritical Reynolds Number," Department of Mechanical Engineering, Technical Report TF-62, Thermo-Sciences Division, Stanford Univ., Stanford, CA, 1994.

[18] Mittal, R., and Moin, P., "Suitability of Upwind-Based Finite Difference Schemes for Large Eddy Simulation of Turbulent Flows," *AIAA Journal*, Vol. 35, No. 8, Aug. 1997, pp. 1415–1417. doi:10.2514/2.253

[19] Breuer, M., "Numerical and Modeling Influences on Large Eddy Simulations for the Flow Past a Circular Cylinder," *International Journal of Heat and Fluid Flow*, Vol. 19, No. 5, Oct. 1998, pp. 512–521. doi:10.1016/S0142-727X(98)10015-2

[20] Kravchenko, A. G., and Moin, P., "B-Spline Methods and Zonal Grids for Numerical Simulation of Turbulent Flows," Department of Mechanical Engineering Report TF-73, Stanford Univ., 1998.

[21] Kravchenko, A. G., and Moin, P., "Numerical Studies of Flow Over a Circular Cylinder at $R_{eD} = 3900$," *Physics of Fluids*, Vol. 12, No. 2, Feb. 2000, pp. 403–417. doi:10.1063/1.870318

[22] Franke, J., and Frank, W., "Large Eddy Simulation of the Flow Past a Circular Cylinder at $Re_D = 3900$," *Journal of Wind Engineering and Industrial Aerodynamics*, Vol. 90, No. 10, Oct. 2002, pp. 1191–1206. doi:10.1016/S0167-6105(02)00232-5

[23] Rizzetta, D. P., Visbal, M. R., and Blaisdell, G. A., "A Time-Implicit High-Order Compact Differencing and Filtering Scheme for Large Eddy Simulation," *International Journal for Numerical Methods in Fluids*, Vol. 42, No. 6, June 2003, pp. 665–693. doi:10.1002/fld.551

[24] Ma, X., Karamanos, G.-S., and Karniadakis, G. E., "Dynamics and Low-Dimensionality of a Turbulent Near Wake," *Journal of Fluid Mechanics*, Vol. 410, May 2000, pp. 29–65. doi:10.1017/S0022112099007934

[25] Jordan, S. A., "Investigation of the Cylinder Separated Shear-Layer Physics by Large Eddy Simulation," *International Journal of Heat and Fluid Flow*, Vol. 23, No. 1, Feb. 2002, pp. 1–12. doi:10.1016/S0142-727X(01)00134-5

[26] Kalro, V., and Tezduyar, T., "Parallel 3D Computation of Unsteady Flows Around Circular Cylinders," *Parallel Computing*, Vol. 23, No. 9, Sept. 1997, pp. 1235–1248. doi:10.1016/S0167-8191(97)00050-1

[27] Dong, S., Karniadakis, G. E., Ekmekci, A., and Rockwell, D., "A Combined Direct Numerical Simulation-Particle Image Velocimetry Study of the Turbulent Near Wake," *Journal of Fluid Mechanics*, Vol. 569, Dec. 2006, pp. 185–207. doi:10.1017/S0022112006002606

[28] Asghar, A., and Jumper, E. J., "Phase Synchronization of Vortex Shedding from Multiple Cylinders Using Plasma Actuators," AIAA Paper 2003-1028, Jan. 2003.

[29] McLaughlin, T. E., Munska, M. D., Vaeth, J. P., Dauwalter, T. E., Goode, J. R., and Siegel, S. G., "Plasma-Based Actuators for Cylinder Wake Vortex Control," AIAA Paper 2004-2129, June–July 2004.

[30] Munska, M. D., and McLaughlin, T. E., "Circular Cylinder Flow Control Using Plasma Actuators," AIAA Paper 2005-141, Jan. 2005.

[31] McLaughlin, T. E., Felker, B., Avery, J. C., and Enloe, C. L., "Further Experiments in Cylinder Wake Modification with Dielectric Barrier Discharge Forcing," AIAA Paper 2006-1409, Jan. 2006.

[32] Thomas, F. O., Kozlov, A., and Corke, T. C., "Plasma Actuators for Landing Gear Noise Reduction," AIAA Paper 2005-3010, May 2005.

[33] Thomas, F. O., Kozlov, A., and Corke, T. C., "Plasma Actuators for Bluff Body Flow Control," AIAA Paper 2006-2845, June 2006.

[34] Roth, J. R., "Aerodynamic Flow Acceleration Using Paraelectric and Peristaltic Electrohydrodynamic Effects of a One Atmosphere Uniform Glow Discharge Plasma," *Physics of Plasmas*, Vol. 10, No. 5, May 2003, pp. 2117–2128. doi:10.1063/1.1564823

[35] Roth, J. R., Sin, H., and Madham, R. C. M., "Flow Re-attachment and Acceleration by Paraelectric and Peristaltic Electrohydrodynamic (EHD) Effects," AIAA Paper 2003-0531, Jan. 2003.

[36] Shyy, W., Jayaraman, B., and Anderson, A., "Modeling of Glow Discharge-Induced Fluid Dynamics," *Journal of Applied Physics*, Vol. 92, No. 11, Dec. 2002, pp. 6434–6443. doi:10.1063/1.1515103

[37] Gaitonde, D. V., Visbal, M. R., and Roy, S., "Control of Flow Past a Wing Section with Plasma-Based Body Forces," AIAA Paper 2005-5302, June 2005.

[38] Visbal, M. R., and Gaitonde, D. V., "Control of Vortical Flows Using Simulated Plasma Actuators," AIAA Paper 2006-0505, Jan. 2005.

[39] Visbal, M. R., Gaitonde, D. V., and Roy, S., "Control of Transitional and Turbulent Flows Using Plasma-Based Actuators," AIAA Paper 2006-3230, June 2006.

[40] Rizzetta, D. P., and Visbal, M. R., "Numerical Investigation of Plasma-Based Flow Control for a Transitional Highly-Loaded Low-Pressure Turbine," AIAA Paper 2007-938, Jan. 2007.

[41] Beam, R., and Warming, R., "An Implicit Factored Scheme for the Compressible Navier-Stokes Equations," *AIAA Journal*, Vol. 16, No. 4, April 1978, pp. 393–402. doi:10.2514/3.60901

[42] Gordnier, R. E., and Visbal, M. R., "Numerical Simulation of Delta-Wing Roll," AIAA Paper 93-0554, Jan. 1993.

[43] Jameson, A., Schmidt, W., and Turkel, E., "Numerical Solutions of the Euler Equations by Finite Volume Methods Using Runge-Kutta Time Stepping Schemes," AIAA Paper 81-1259, June 1981.

[44] Pulliam, T. H., and Chaussee, D. S., "A Diagonal Form of an Implicit Approximate-Factorization Algorithm," *Journal of Computational Physics*, Vol. 39, No. 2, Feb. 1981, pp. 347–363. doi:10.1016/0021-9991(81)90156-X

[45] Lele, S. A., "Compact Finite Difference Schemes with Spectral-like Resolution," *Journal of Computational Physics*, Vol. 103, No. 1, Nov. 1992, pp. 16–42. doi:10.1016/0021-9991(92)90324-R

[46] Visbal, M. R., and Gaitonde, D. V., "High-Order-Accurate Methods for Complex Unsteady Subsonic Flows," *AIAA Journal*, Vol. 37, No. 10, Oct. 1999, pp. 1231–1239. doi:10.2514/2.591

[47] Gaitonde, D., Shang, J. S., and Young, J. L., "Practical Aspects of High-Order Accurate Finite-Volume Schemes for Electromagnetics," AIAA Paper 97-0363, Jan. 1997.

[48] Gaitonde, D., and Visbal, M. R., "High-Order Schemes for Navier-Stokes Equations: Algorithm and Implementation into FDL3DI," Air Force Research Laboratory, Technical Report AFRL-VA-WP-TR-1998-3060, Wright–Patterson Air Force Base, OH, Aug. 1998.

[49] Gordnier, R. E., "Computation of Delta-Wing Roll Maneuvers," *Journal of Aircraft*, Vol. 32, No. 3, May 1995, pp. 486–492. doi:10.2514/3.46746

[50] Visbal, M. R., "Computational Study of Vortex Breakdown on a Pitching Delta Wing," AIAA Paper 93-2974, July 1993.

[51] Visbal, M., Gaitonde, D., and Gogineni, S., "Direct Numerical Simulation of a Forced Transitional Plane Wall Jet," AIAA Paper 98-2643, June 1998.

[52] Rizzetta, D. P., Visbal, M. R., and Stanek, M. J., "Numerical Investigation of Synthetic-Jet Flowfields," *AIAA Journal*, Vol. 37, No. 8, Aug. 1999, pp. 919–927. doi:10.2514/2.811

[53] Rizzetta, D. P., and Visbal, M. R., "Direct Numerical Simulation of Flow Past an Array of Distributed Roughness Elements," AIAA Paper 2006-3527, June 2006.

[54] Rizzetta, D. P., and Visbal, M. R., "Numerical Investigation of Transitional Flow Through a Low-Pressure Turbine Cascade," AIAA Paper 2003-3587, June 2003.

[55] Rizzetta, D. P., and Visbal, M. R., "Application of Large Eddy Simulation to Supersonic Compression Ramps," *AIAA Journal*, Vol. 40, No. 8, Aug. 2002, pp. 1574–1581. doi:10.2514/2.1826

[56] Rizzetta, D. P., and Visbal, M. R., "Large Eddy Simulation of Supersonic Cavity Flowfields Including Flow Control," *AIAA Journal*, Vol. 41, No. 8, Aug. 2003, pp. 1452–1462. doi:10.2514/2.2128

[57] Visbal, M. R., and Rizzetta, D. P., "Large Eddy Simulation on Curvilinear Grids Using Compact Differencing and Filtering Schemes," *Journal of Fluids Engineering*, Vol. 124, No. 4, Dec. 2002, pp. 836–847. doi:10.1115/1.1517564

[58] Visbal, M. R., Morgan, P. E., and Rizzetta, D. P., "An Implicit LES Approach Based on High-Order Compact Differencing and Filtering Schemes," AIAA Paper 2003-4098, June 2003.

[59] Fureby, C., and Grinstein, F. F., "Monotonically Integrated Large Eddy Simulation," *AIAA Journal*, Vol. 37, No. 5, May 1999, pp. 544–556. doi:10.2514/2.772

[60] Stoltz, S., and Adams, N. A., "An Approximate Deconvolution Procedure for Large Eddy Simulation," *Physics of Fluids*, Vol. 11, No. 7, July 1999, pp. 1699–1701. doi:10.1063/1.869867

[61] Mathew, J., Lechner, R., Foysi, H., Sesterhenn, J., and Friedrich, R., "An Explicit Filtering Method for Large Eddy Simulation of Compressible Flows," *Physics of Fluids*, Vol. 15, No. 8, Aug. 2003, pp. 2279–2289. doi:10.1063/1.1586271

[62] Sherer, S. E., "Further Analysis of High-Order Overset Grid Method with Applications," AIAA Paper 2003-3839, June 2003.

[63] Sherer, S. E., and Visbal, M. R., "Multi-Resolution Implicit Large Eddy Simulations Using a High- Order Overset-Grid Approach," *International Journal for Numerical Methods in Fluids*, Vol. 55, March 2007, pp. 455–482. doi:10.1002/fld.1463

[64] Rizzetta, D. P., and Visbal, M. R., "Direct Numerical Simulation of Flow Past an Array of Distributed Roughness Elements," *AIAA Journal*, Vol. 45, No. 8, Aug. 2007, pp. 1967–1976. doi:10.2514/1.25916

[65] Rizzetta, D. P., and Visbal, M. R., "Numerical Investigation of Plasma-Based Flow Control for Transitional Highly Loaded Low-Pressure Turbine," *AIAA Journal*, Vol. 45, No. 10, Oct. 2007, pp. 2554–2564. doi:10.2514/1.29602

[66] Visbal, M. R., and Gaitonde, D. V., "Very High-Order Spatially Implicit Schemes for Computational Acoustics on Curvilinear Meshes," *Journal of Computational Acoustics*, Vol. 9, No. 4, Dec. 2001, pp. 1259–1286.

[67] Corke, T. C., and Post, M. L., "Overview of Plasma Flow Control: Concepts, Optimization, and Applications," AIAA Paper 2005-0563, Jan. 2005.

[68] Rizzetta, D. P., and Visbal, M. R., "Numerical Study of Active Flow Control for a Transitional Highly- Loaded Low-Pressure Turbine," Journal of Fluids Engineering, Vol. 128, No. 5, Sept. 2006, pp. 956–967.

[69] Rizzetta, D. P., and Visbal, M. R., "Numerical Simulation of Separation Control for Transitional Highly-Loaded Low-Pressure Turbines," *AIAA Journal*, Vol. 43, No. 9, Sept. 2005, pp. 1958–1967. doi:10.2514/1.12376

[70] Suhs, N. E., Rogers, S. E., and Dietz, W. E., "PEGASUS 5: An Automated Preprocessor for Overset-Grid Computational Fluid Dynamics," *AIAA Journal*, Vol. 41, No. 6, June 2003, pp. 1037–1045. doi:10.2514/2.2070

[71] "MPI: A Message-Passing Interface Standard," Message Passing Interface Forum, Computer Science Department, Technical Report CS-94-230, Univ. of Tennessee, Knoxville, TN, April 1994.

P. Givi
Associate Editor